

# Supporting Information

## **Composition-Tunable Synthesis of “Clean” Syngas via One-Step Synthesized Metal-Free Pyridinic-N Enriched Self-Supported CNTs: The Synergy of Electrocatalysts and Potential**

Kai-hua Liu<sup>a,b</sup>, Hai-xia Zhong<sup>a</sup>, Xiao-yang Yang<sup>a,b</sup>, Di Bao<sup>a</sup>, Fan-lu Meng<sup>a,b</sup>, Jun-min Yan<sup>b\*</sup>, and Xin-bo Zhang<sup>a</sup>

<sup>a</sup>Key Laboratory of Automobile Materials (Jilin University), Ministry of Education, Department of Materials Science and Engineering, Jilin University, Changchun, 130022, China

<sup>b</sup>State Key Laboratory of Rare Earth Resource Utilization, Changchun Institute of Applied Chemistry, Chinese Academy of Sciences, Changchun, 130022, P. R. China

\*E-mail: junminyan@jlu.edu.cn

## **Experimental**

### **1. Materials Preparation**

**Synthesis of N-CNTs/SS-750:** The preparation of N-CNTs/SS-750 was achieved via in situ growth of the N-CNTs on SS with only melamine both as the nitrogen and carbon sources under 750 °C. Briefly, the SS was cleaned by sonication in ethanol for 10 min and then dried at 80 °C. The SS (304, thickness: 0.070 mm) was propped on a porcelain boat which was filled with about 2.5 g melamine powder (Under the low concentration, the NCNTs cannot be synthesized, while at high concentration, the NCNTs will dehisce and steel substrate will be fragile as shown in Figure S2). Subsequently, the samples were heated at 750 °C for 180 min in a flowing Ar atmosphere, and then naturally cooled to ambient temperature under Ar. The loading of NCNTs is about 4 mg cm<sup>-2</sup> based on the mass difference before and after the melamine treatment using a microbalance. The synthesis procedure of other samples was the same as N-CNTs/SS-750 with only the carbonization temperature changed.

### **2. Physicochemical Characterization**

Powder X-ray diffraction (XRD) measurement was performed using a Bruker D8 Focus Power X-ray diffractometer with Cu K $\alpha$  ( $\lambda = 0.15405$  nm) radiation (40 kV, 40 mA). Scanning electron microscopy (SEM) and elemental-mapping were carried out with a field emission scanning electron microanalyzer (Hitachi S4800) operating at an accelerating voltage of 10 kV. Transmission electron microscope (TEM) was performed on a FEI Tecnai G2 S-Twin instrument with a field

emission gun operating at 200 kV. Raman spectra were collected with a Renishaw 2000 model confocal microscopy Raman spectrometer with a CCD detector and a holographic notch filter at ambient conditions. X-ray photoelectron spectroscopy (XPS) analysis was carried on a VG Scientific ESCALAB MKII X-ray photoelectron spectrometer using an Al K $\alpha$  source. Electrochemical measurements were performed using a BioLogic VMP3 electrochemical workstation at room temperature. NMR spectra were recorded on Bruker NMR spectrometers (AVANCE-III HD 500). Gas components analysis was performed on gas chromatograph (ThermoFisher Trace 1300) with pulsed discharge detector (PDD) and flame ionization detector (FID). The electron conductivity is obtained from Four-Point-Probe-RTS-9.

### **3. Electrochemical Characterization**

Electrochemical measurements were carried out in an H-cell (separated by Nafion 211) system. The synthesized N-CNTs/SS were directly used as working electrode. The Pt wire and Ag/AgCl electrode were used as the counter electrode and reference electrode, respectively. Some potentials were converted to the RHE scale via calibration ( $E_{\text{RHE}} = E_{\text{Ag/AgCl}} + 0.059\text{pH} + 0.197$ ). For CO<sub>2</sub> reduction experiments, cyclic voltammetry with a scan rate of 20 mV s<sup>-1</sup> was conducted in Ar or CO<sub>2</sub>-saturated 0.1 M KHCO<sub>3</sub> solution (the KHCO<sub>3</sub> electrolyte was purged with Ar or CO<sub>2</sub> for at least 30 min before the measurement).

The electrochemical double layer capacitances ( $C_{\text{dl}}$ ) of catalysts are measured by using a simple cyclic voltammetry method. It is known that the  $C_{\text{dl}}$  value is

expected to be linearly proportional to the electrochemically active surface area of the electrode. The potential window of cyclic voltammetric stripping was 0.4 V to 0.3 V versus Ag/AgCl (0.1 M KHCO<sub>3</sub> solution). The scan rates were 2, 6, 12, 18, 24 and 30 mV s<sup>-1</sup>. Then, The C<sub>dl</sub> was estimated by plotting the  $\Delta j = (j_a - j_c)/2$  at 0.35 V (where j<sub>a</sub> and j<sub>c</sub> were the anodic and cathodic current densities, respectively) versus Ag/AgCl against the scan rate, in which the slope was the C<sub>dl</sub>.

During the CO<sub>2</sub> reduction experiments, CO<sub>2</sub> gas was delivered at an average rate of 30 ml/min (at room temperature and ambient pressure) and routed directly into the gas sampling loop of a gas chromatograph (ThermoFisher Trace 1300). The gas phase composition was analyzed by GC every 20 min. The GC analysis was set up to split the gas sample into two aliquots where of one aliquot was routed through a packed MoleSieve 5A column and a packed Rt-Q-BOND column before passing a pulsed discharge detector (PDD) for CO quantification. Helium and nitrogen were employed as carrier or make-up gases, respectively. The second aliquot was routed through a packed Rt-Q-BOND column equipped with a flame ionization detector (FID) for analyzing all major C<sub>2</sub> to C<sub>4</sub> hydrocarbons. The GC was calibrated using commercially available calibration standards from Guangming Research & Design Institute of Chemical Industry.

<sup>1</sup>H NMR spectroscopy (Bruker AVANCE-III HD 500) was employed at the end of experiments to test for possible production of liquid products, in which 0.5 ml electrolyte was mixed with 0.1 ml D<sub>2</sub>O and 0.05 μl dimethyl sulfoxide (DMSO, Sigma, 99.9%) was added as an internal standard.

The partial current densities associated with production of CO and H<sub>2</sub> were calculated from the GC peak area as follows:<sup>1</sup>

$$J_{CO} = \frac{\text{Peak Area}}{a} \times \text{Flow Rate} \times \frac{2FP_0}{RT} \times (\text{Electrode Area})^{-1}$$

$$J_{H_2} = \frac{\text{Peak Area}}{\beta} \times \text{Flow Rate} \times \frac{2FP_0}{RT} \times (\text{Electrode Area})^{-1}$$

Where  $a$  and  $\beta$  are the conversion factors based on calibration of the GC with standard samples of CO and H<sub>2</sub>, respectively.  $F = 96485 \text{ C mol}^{-1}$ ,  $P_0 = 1 \text{ atm}$ ,  $R = 82.1 \text{ ml atm k}^{-1} \text{ mol}^{-1}$ , and  $T = 300 \text{ K}$ . Faradaic efficiencies for a given product were calculated by dividing these partial current densities by the total current density.

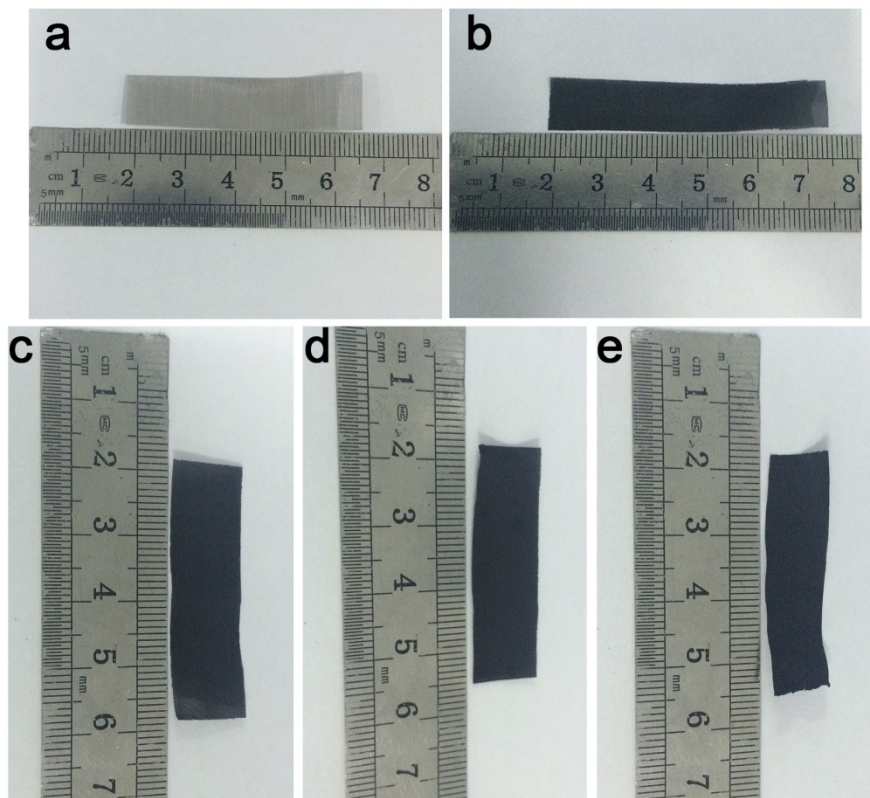


**Figure S1.** Photographs of pure SS (a), N-CNTs/SS-650 (b), N-CNTs/SS-700 (c), N-CNTs/SS-750 (d) and N-CNTs/SS-800 (e).

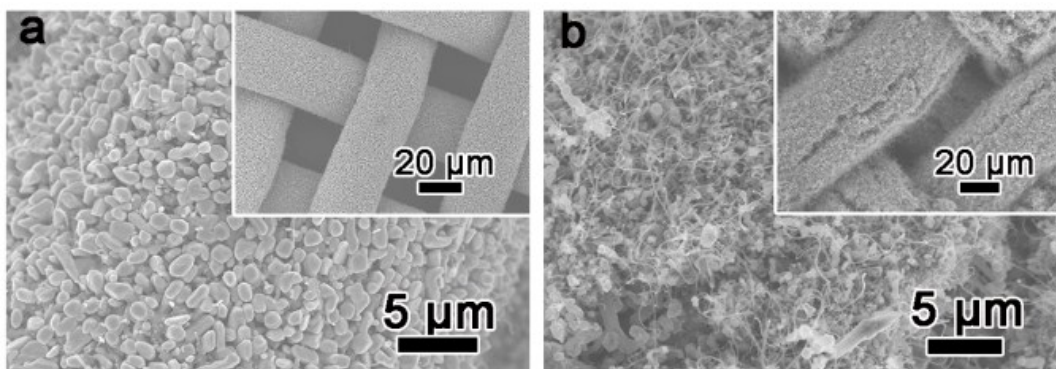


**Figure S2.** SEM images of N-CNTs/SS-750 with 1 g melamine powder (a), N-CNTs/SS-750 with 4 g melamine powder (b).

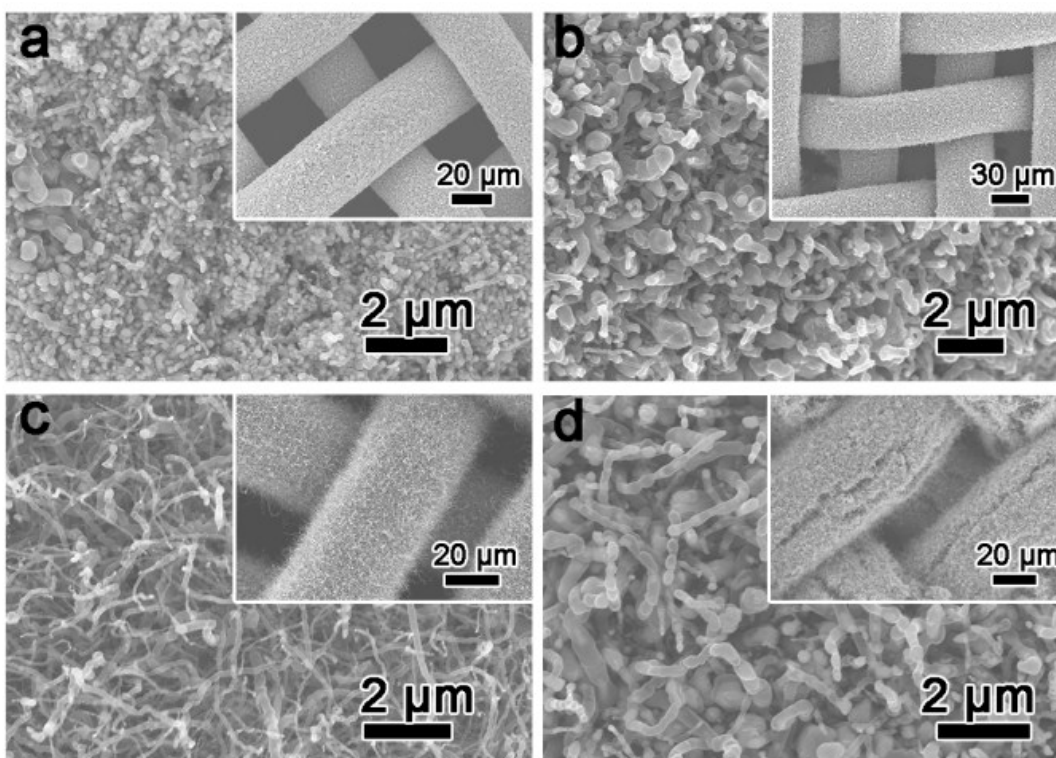


**Figure S3.** SEM images of N-CNTs/SS-650 (a), N-CNTs/SS-700 (b), N-CNTs/SS-750 (c) and N-CNTs/SS-800 (d).

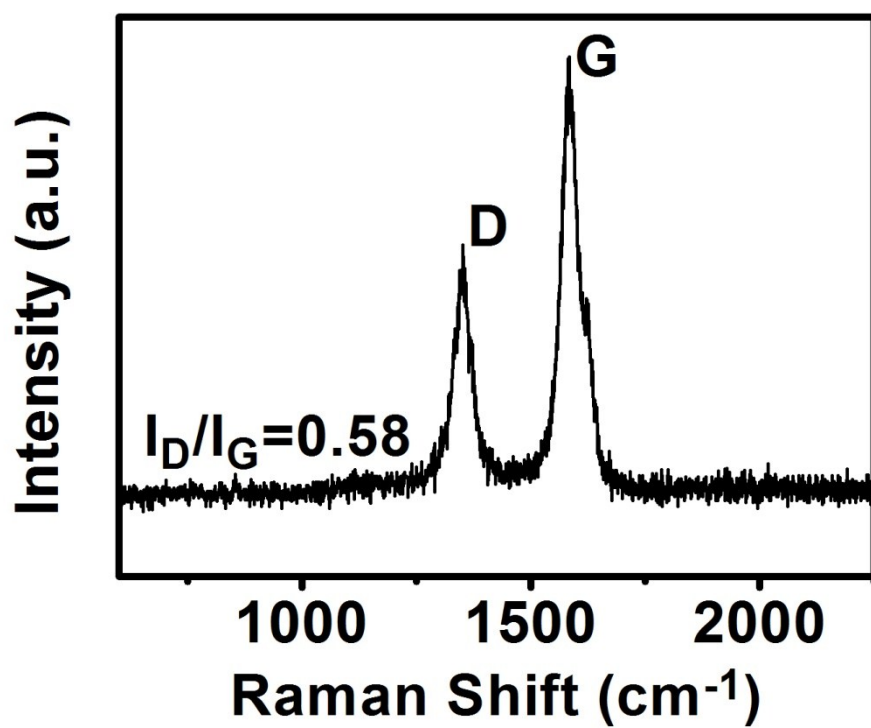


**Figure S4.** The Raman spectrum of pure commercial CNTs.

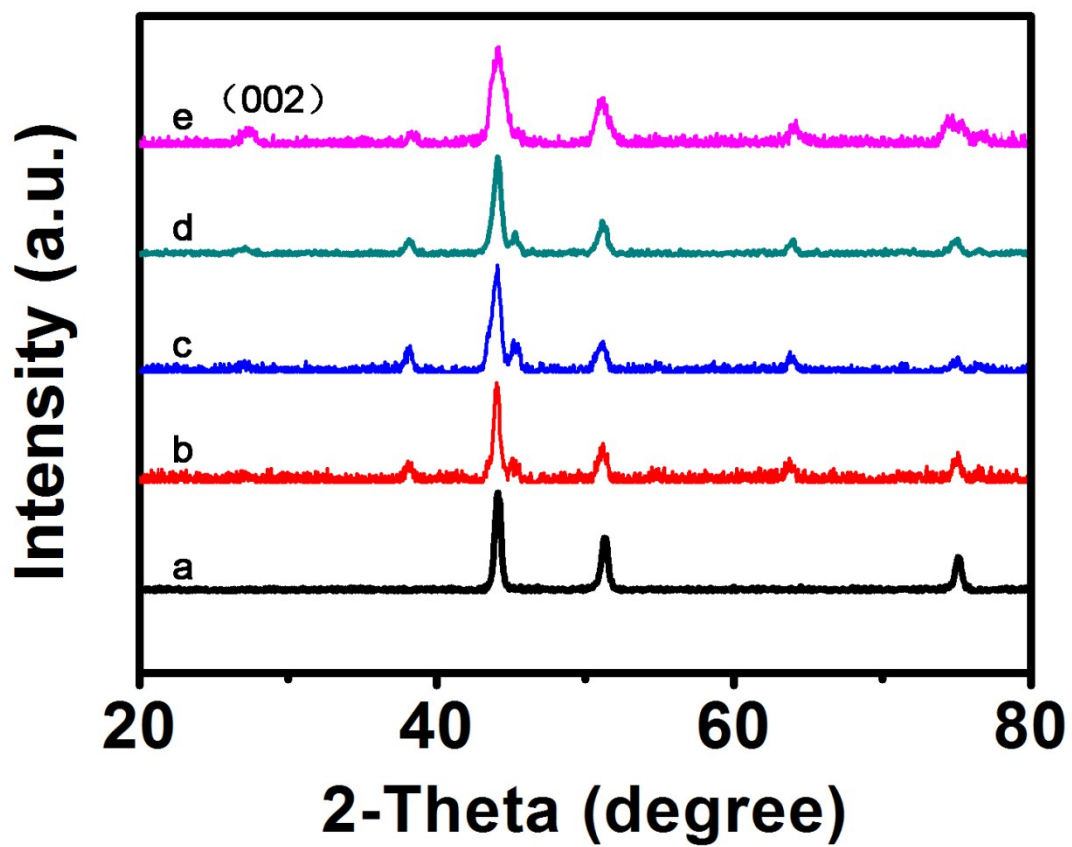


**Figure S5.** The XRD patterns of SS (a), N-CNTs/SS-650 (b), N-CNTs/SS-700 (c), N-CNTs/SS-750 (d) and N-CNTs/SS-800 (e).

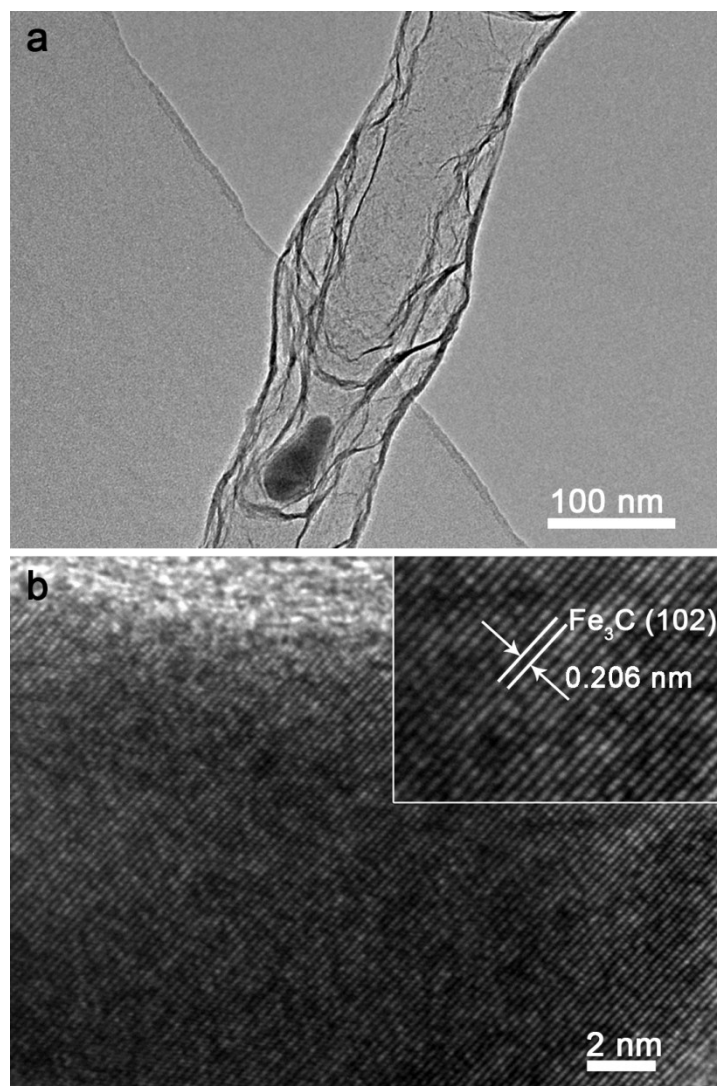


**Figure S6.** The TEM (a) and HRTEM (b) images of synthesized N-CNTs/SS.

Based on the XRD patterns, TEM and HRTEM images of synthesized N-CNTs, some Fe<sub>3</sub>C nanoparticles are embedded in some carbon nanotubes. However, as the interface reaction and lack of access to electrolyte, the extremely few Fe<sub>3</sub>C nanoparticles presumably does not contribute to CO<sub>2</sub> reduction. Thus, the produced gas products of CO<sub>2</sub> reduction is attributed to the N-CNTs.

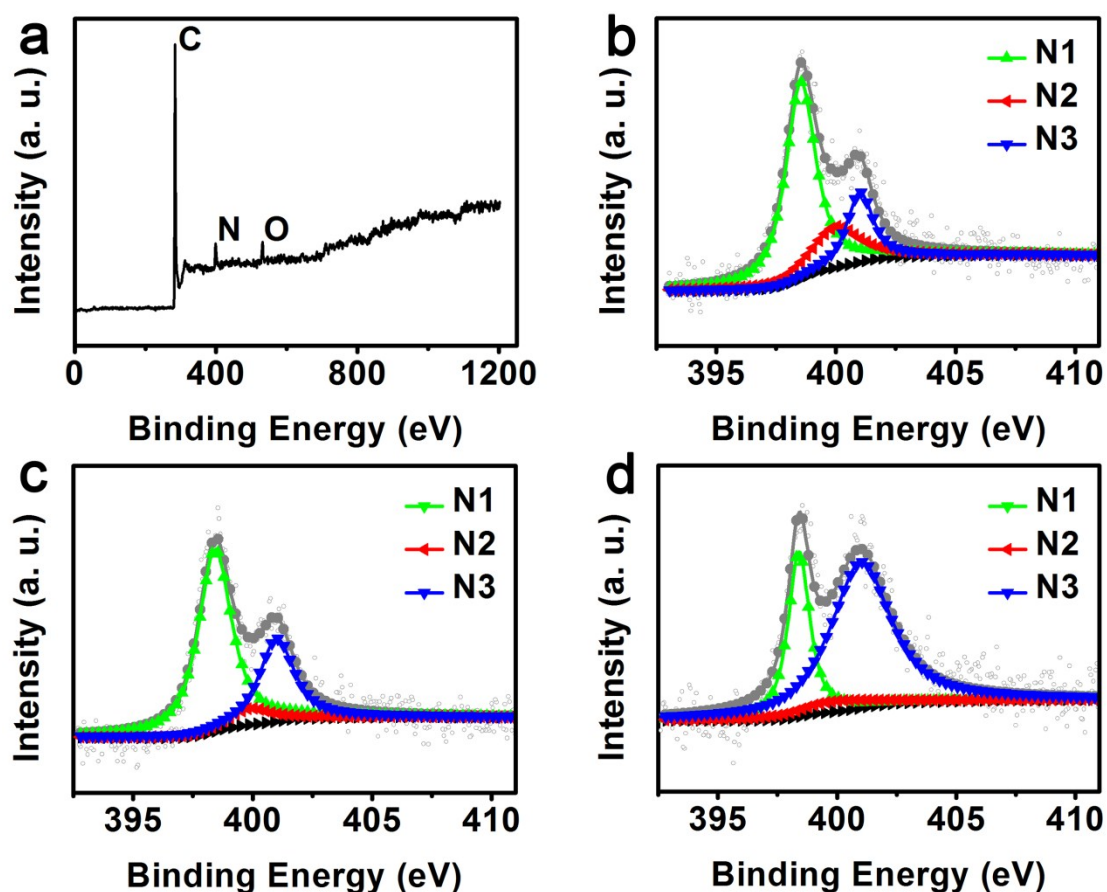


**Figure S7.** survey spectrum of XPS (a), N 1s XPS spectra for N-CNTs/SS-650, N-CNTs/SS-700 and N-CNTs/SS-800 (b-d), respectively.

The survey spectra of N-CNTs clearly shows the N peak at around 400 eV in addition to a dominant graphitic C peak at 284.5 eV. And three different bonding states of N at 398.4, 399.9, and 401.1 eV, corresponding to N1, N2 and N3, are also discovered in the fitted high resolution of N 1s peaks of different samples based on the standard XPS binding energy table and references.<sup>2-4</sup>

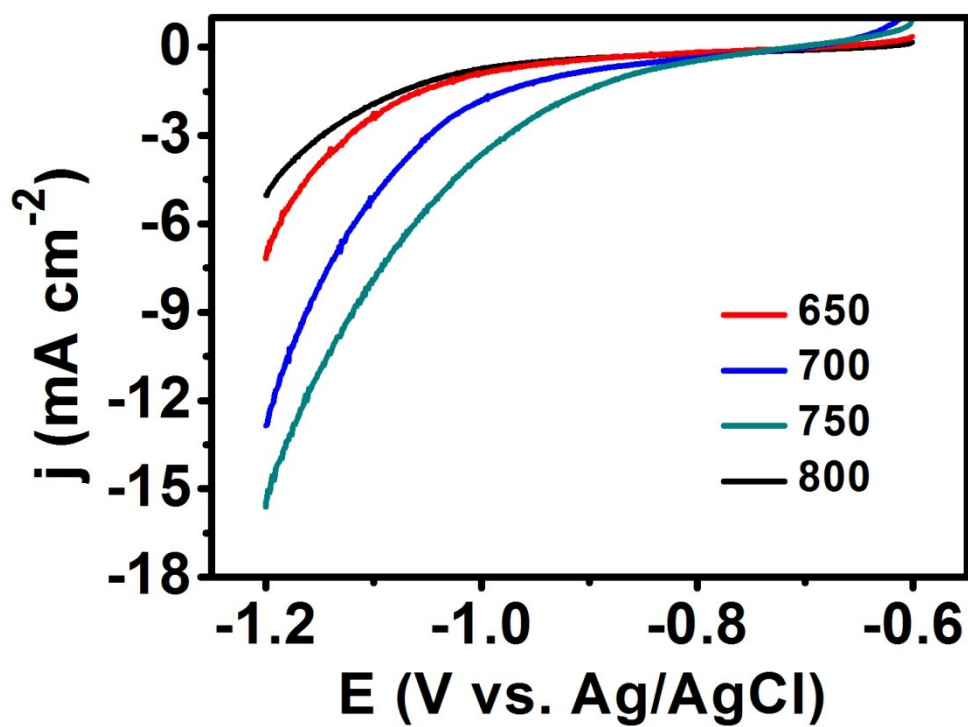


**Figure S8.** Linear sweep voltammetric curves in the  $\text{CO}_2$ -saturated 0.1 M  $\text{KHCO}_3$  aqueous solution.

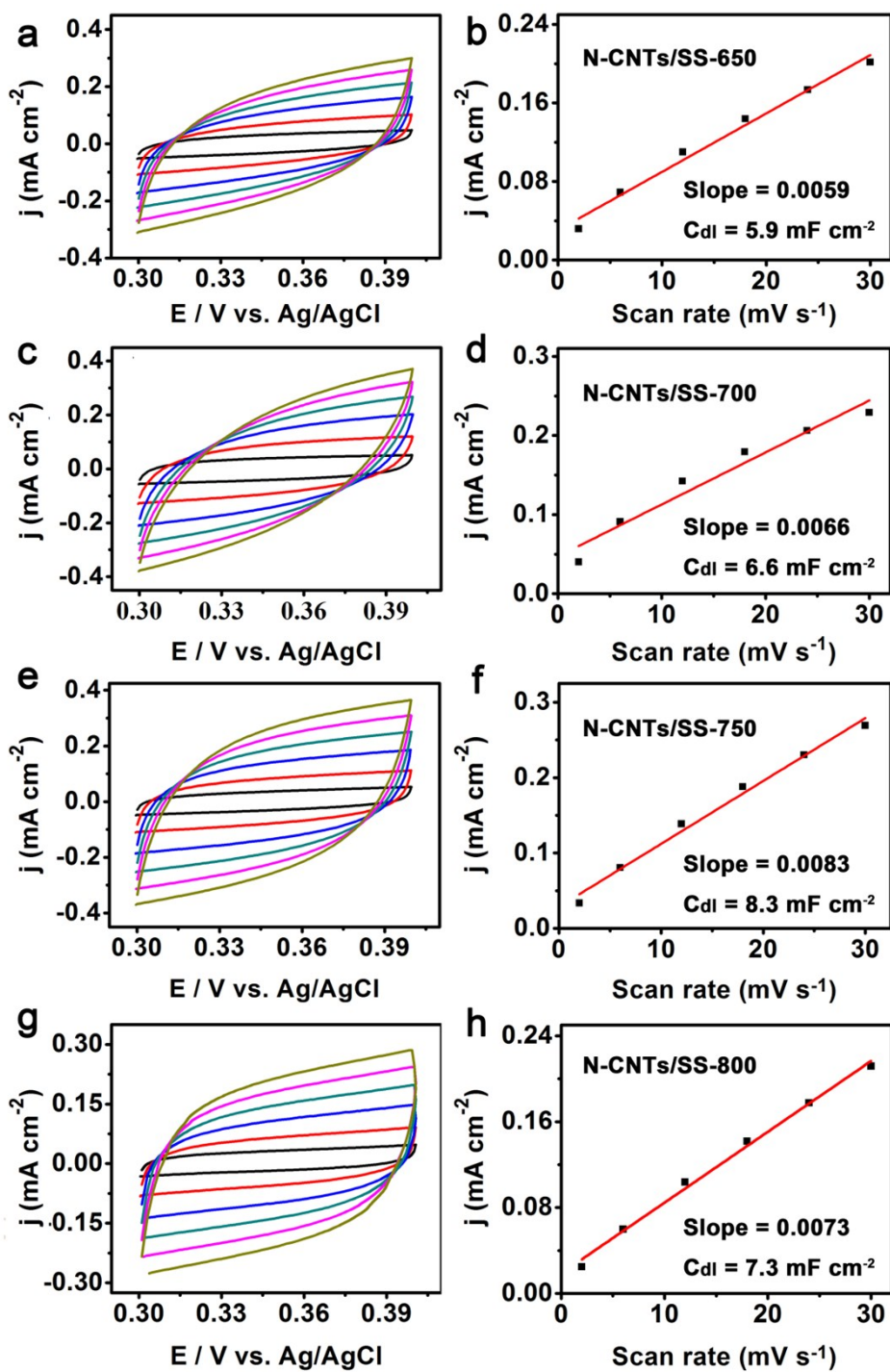


**Figure S9.** Cyclic voltammograms in the region of 0.30-0.40 V vs. Ag/AgCl at various scan rates and the corresponding linear fitting plots of the capacitive currents vs. scan rates to estimate the  $C_{dl}$ . (a) and (b) for N-CNTs/SS-650; (c) and (d) for N-CNTs/SS-700; (e) and (f) for N-CNTs/SS-750; (g) and (h) for N-CNTs/SS-800, and the calculated  $C_{dl}$  values are shown in the insets.

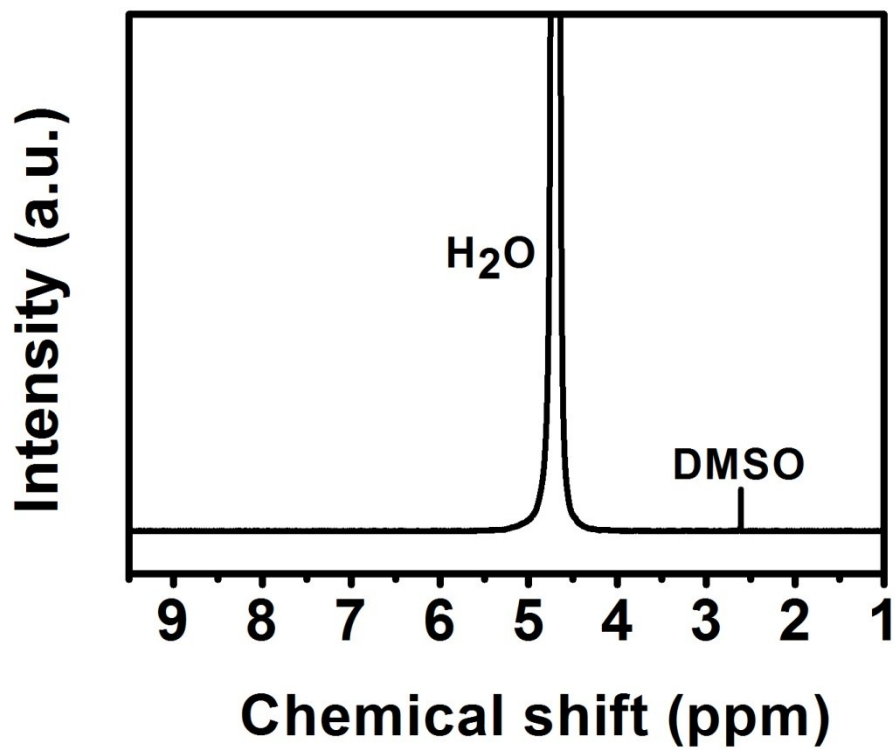


**Figure S10.** Representative NMR spectra of the electrolyte after CO<sub>2</sub> reduction electrolysis at -1.1 V versus Ag/AgCl for the N-CNTs/SS-750. DMSO is used as an internal standard.

From the <sup>1</sup>H NMR spectra, no liquid products peaks are detected except the H<sub>2</sub>O and DMSO, indicating the CO<sub>2</sub> reduction products only gas components.

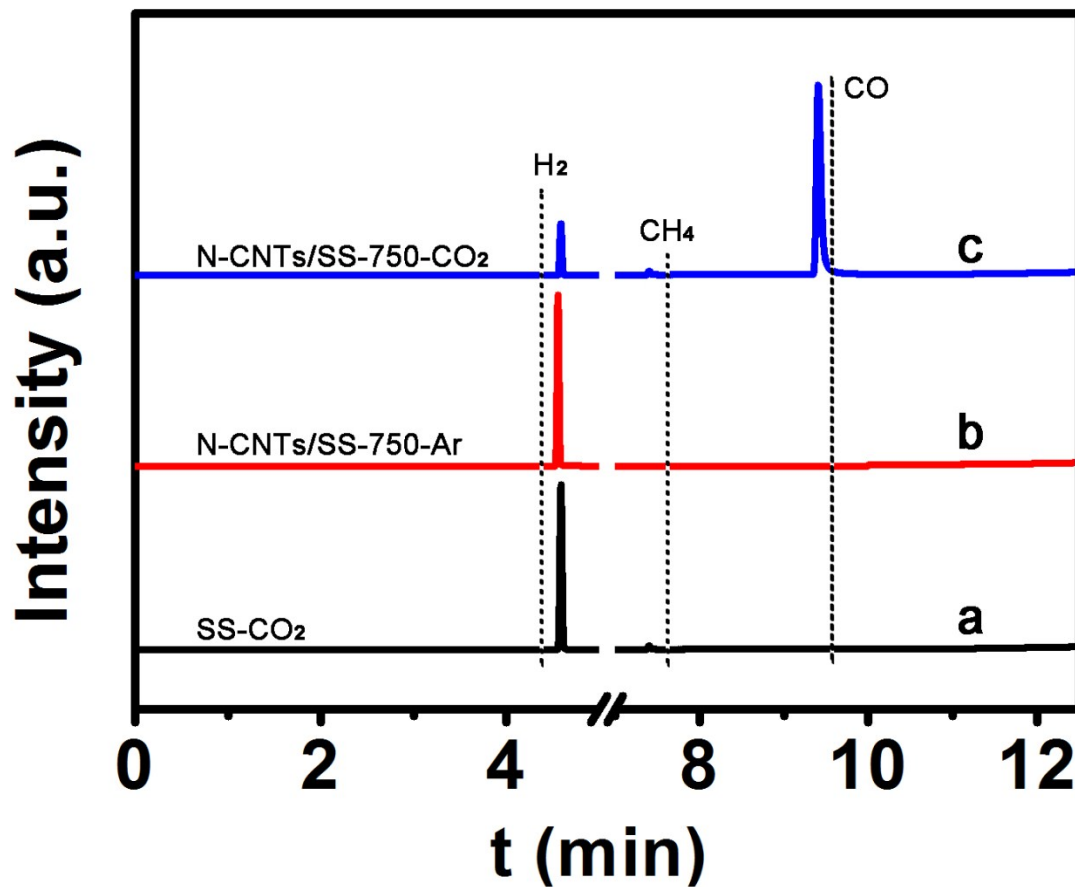


**Figure S11.** GC spectrum using PDD for the produced gas over SS in CO<sub>2</sub> saturated KHCO<sub>3</sub> solution (a), N-CNTs/SS-750 in Ar saturated KHCO<sub>3</sub> solution (b) and the N-CNTs/SS-750 in CO<sub>2</sub> saturated KHCO<sub>3</sub> solution (c) at -1.1 V vs. Ag/AgCl.

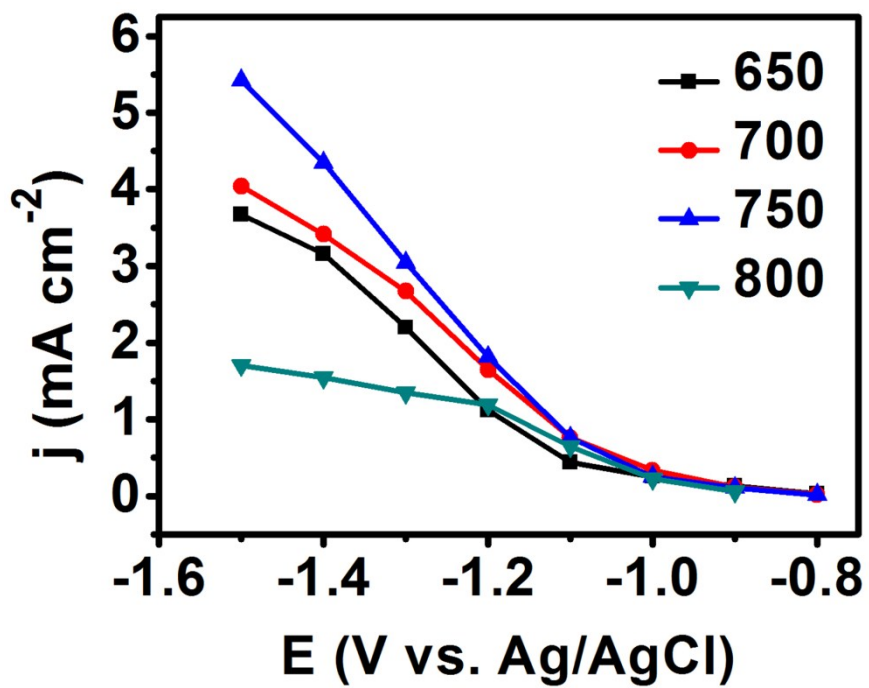
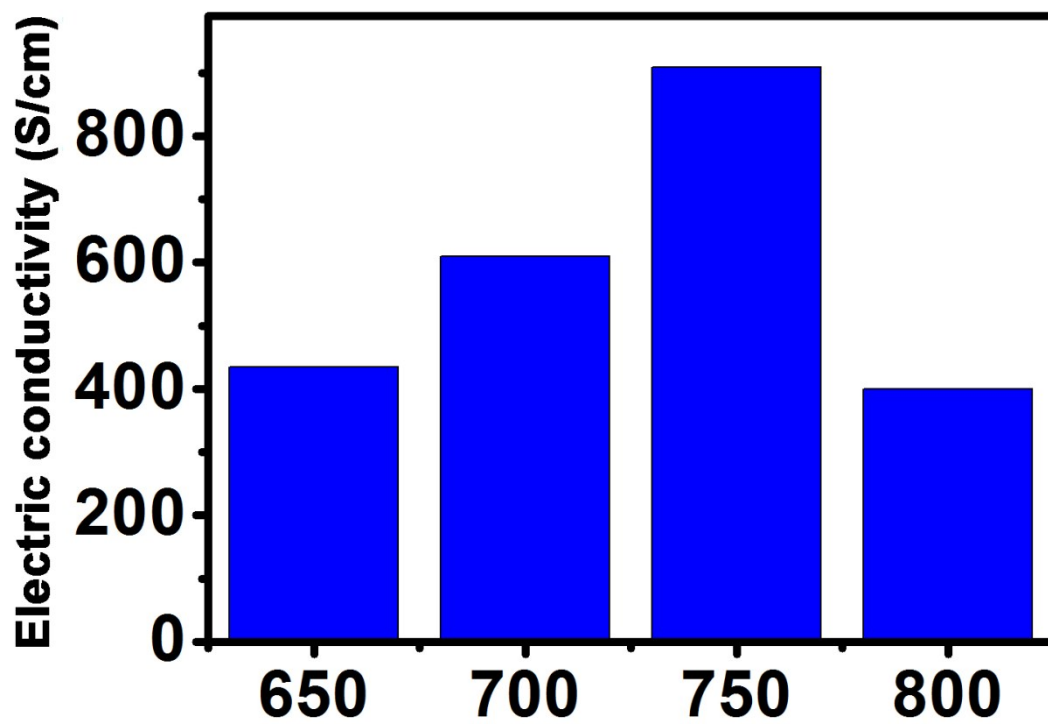
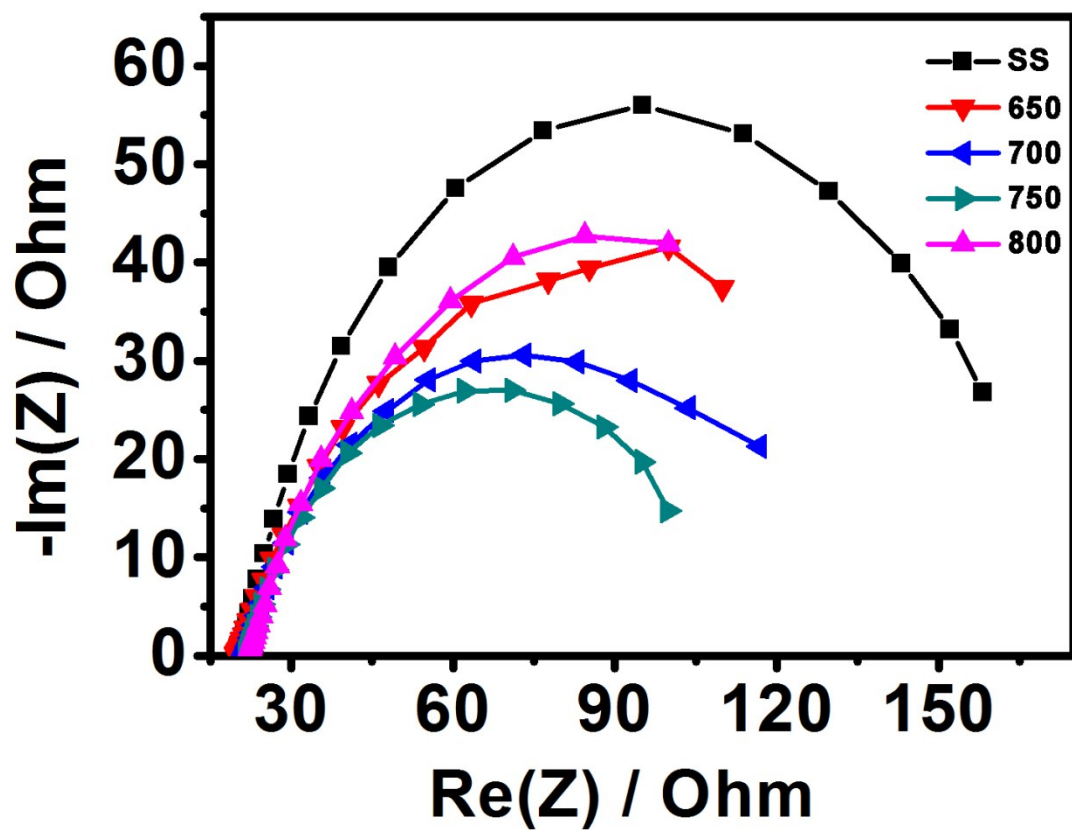


Figure S12. Partial current density of CO versus potential.



**Figure S13.** The electric conductivity of N-CNTs/SS-650, N-CNTs/SS-700, N-CNTs/SS-750 and N-CNTs/SS-800.



**Figure S14.** The electrochemical impedance plots obtained at a potential of -1.0 V vs. Ag/AgCl.

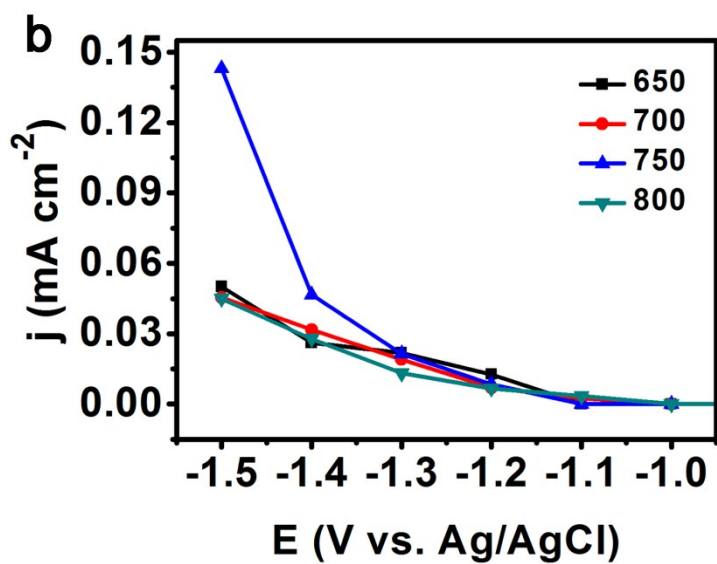
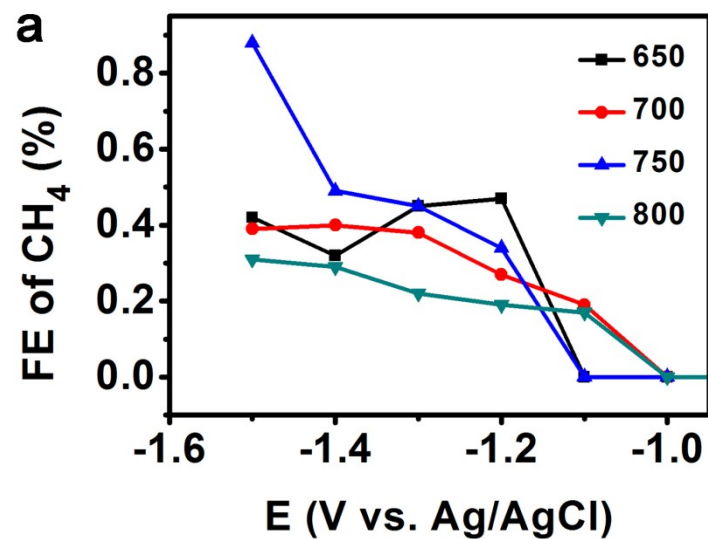


**Figure S15.** The Faradaic efficiency of CH<sub>4</sub> (a) and partial current density of CH<sub>4</sub> versus potential (b).

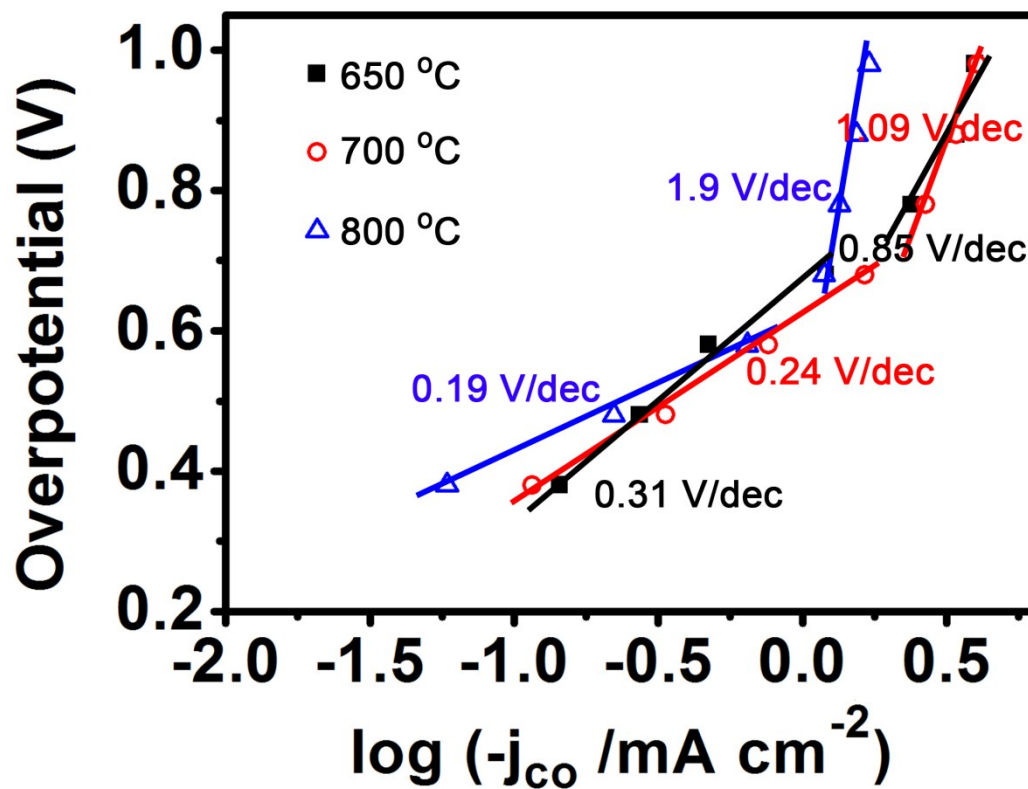
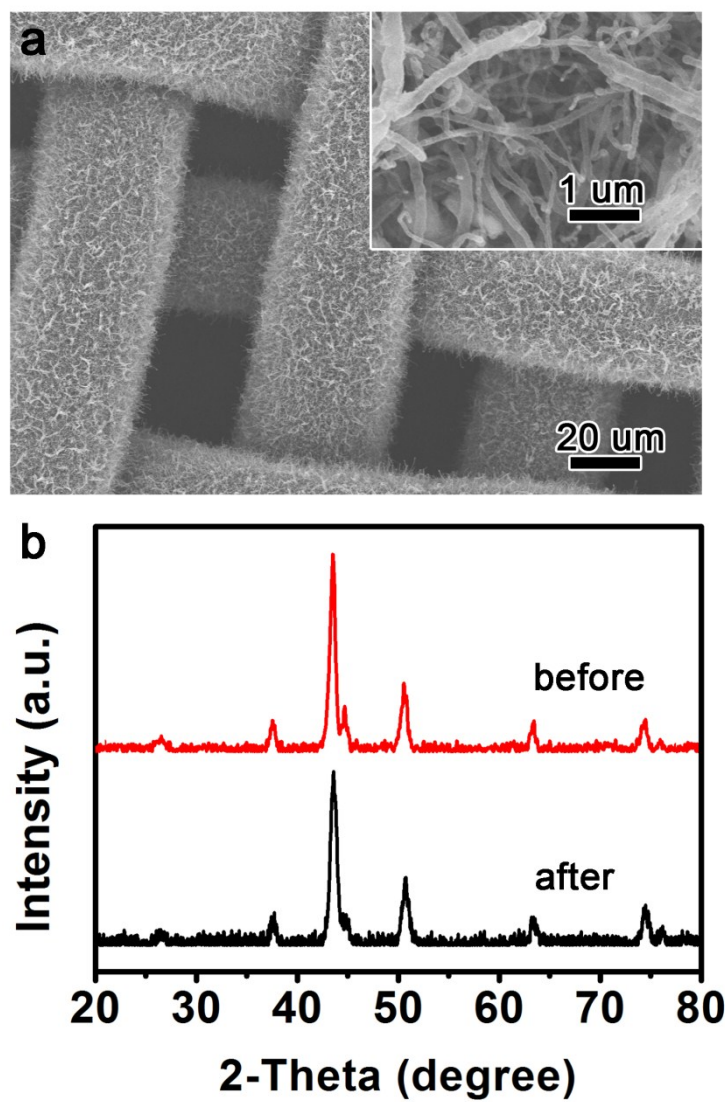
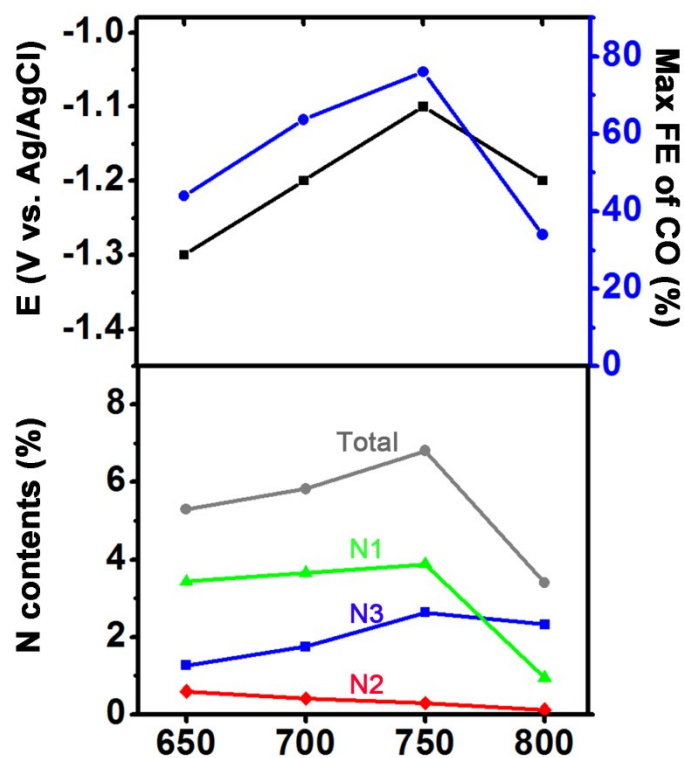


Figure S16. Tafel plots of N-CNTs/SS electrodes for CO<sub>2</sub> reduction.



**Figure S17.** The SEM image of N-CNTs/SS-750 after long-term stability test (a) and the XRD patterns of N-CNTs/SS-750 before and after stability test (b).



**Figure S18.** Maximum Faradaic efficiency of CO and its corresponding potential versus N functionality contents.

As shown in this Figure, the pyridinic-N and graphitic-N all have the positive effect on the CO<sub>2</sub> reduction, which corresponds with the previous reports.<sup>3,4</sup> And significantly, the pyridinic-N and graphitic-N, especially the pyridinic-N, are the predominant contents in our synthesized the integrated N-CNTs/SS electrode.

**Table S1.** Total N contents of different samples tested by XPS and Element analysis.

	N-CNTs/SS-650	N-CNTs/SS-700	N-CNTs/SS-750	N-CNTs/SS-800
XPS	5.30	5.82	6.81	3.40
Element analysis	5.05	5.54	6.36	3.86

To measure the change of total N contents accurately, the XPS and element analysis were performed to probe the nitrogen concentration, respectively. As a result, the variation trend was the same that the total N contents increased before 750 °C and then decreased.

**Table S2.** Comparison of various electrocatalysts for CO<sub>2</sub> reduction is summarized (mainly selective CO production).

Catalysts	Electrolyte	Potential (V vs. RHE)	Current Density (mA cm <sup>-2</sup> )	Products (FE %)	Stability	Ref.
Ag	0.1 M KHCO <sub>3</sub>	-1.02	—	CO (90%)	—	5
Au (8 nm)	0.5 M KHCO <sub>3</sub>	-0.67	—	CO (90%)	—	6
Au (3.2 nm)	0.1 M KHCO <sub>3</sub>	-1.2	100	CO (20%)	—	7
Au <sub>3</sub> Cu	0.1 M KHCO <sub>3</sub>	-0.73	3	CO (64.7%)	—	8
Cu-In	0.1 M KHCO <sub>3</sub>	-0.6	0.7	CO (85%)	7 h	9
Cu (10 nm)	0.1 M KHCO <sub>3</sub>	-1.1	20	CO (22%)	—	10
Cu-ZnO	0.5M KHCO <sub>3</sub>	-0.23	4	CO (35%)	10 h	11
Zn	0.5 M NaHCO <sub>3</sub>	-1.1	18	CO (79%)	3 h	12
Fe-N-carbon	0.1 M KHCO <sub>3</sub>	-0.5	3	CO (80%)	—	13
NCNT	0.1 M KHCO <sub>3</sub>	-0.2	0.9	CO (80%)	10 h	2
N-graphene foam	0.1 M KHCO <sub>3</sub>	-0.58	1.8	CO (80%)	5 h	4
N-graphene	0.5 M KHCO <sub>3</sub>	-0.84	7.3	formate (73%)	12 h	14
N-CNTs/SS	0.1 M KHCO <sub>3</sub>	-0.5	1.8	CO (75%)	8 h	This study

## Reference

1. C. W. Li and M. W. Kanan, *J. Am. Chem. Soc.*, 2012, **134**, 7231-7234.
2. J. Wu, R. M. Yadav, M. Liu, P. P. Sharma, C. S. Tiwary, L. Ma, X. Zou, X.-D. Zhou, B. I. Yakobson, J. Lou and P. M. Ajayan, *Acs Nano*, 2015, **9**, 5364-5371.
3. P. P. Sharma, J. Wu, R. M. Yadav, M. Liu, C. J. Wright, C. S. Tiwary, B. I. Yakobson, J. Lou, P. M. Ajayan and X.-D. Zhou, *Angew. Chem. Int. Ed.*, 2015, **54**, 13701-13705.
4. J. Wu, M. Liu, P. P. Sharma, R. M. Yadav, L. Ma, Y. Yang, X. Zou, X.-D. Zhou, R. Vajtai, B. I. Yakobson, J. Lou and P. M. Ajayan, *Nano Lett.*, 2016, **16**, 466-470.
5. T. Hatsukade, K. P. Kuhl, E. R. Cave, D. N. Abram and T. F. Jaramillo, *Phys. Chem. Chem. Phys.*, 2014, **16**, 13814-13819.
6. W. Zhu, R. Michalsky, O. Metin, H. Lv, S. Guo, C. J. Wright, X. Sun, A. A. Peterson and S. Sun, *J. Am. Chem. Soc.*, 2013, **135**, 16833-16836.
7. H. Mistry, R. Reske, Z. Zeng, Z. J. Zhao, J. Greeley, P. Strasser and B. R. Cuenya, *J. Am. Chem. Soc.*, 2014, **136**, 16473-16476.
8. D. Kim, J. Resasco, Y. Yu, A. M. Asiri and P. Yang, *Nat. Commun.*, 2014, **5**.
9. S. Rasul, D. H. Anjum, A. Jedidi, Y. Minenkoy, L. Cavallo and K. Takanebe, *Angew. Chem. Int. Ed.*, 2015, **54**, 2146-2150.
10. R. Reske, H. Mistry, F. Behafarid, B. R. Cuenya and P. Strasser, *J. Am. Chem. Soc.*, 2014, **136**, 6978-6986.
11. S. Chu, S. Fan, Y. Wang, D. Rossouw, Y. Wang, G. A. Botton and Z. Mi, *Angew Chem Int Ed Engl*, 2016, **55**, 14262-14266.
12. J. Rosen, G. S. Hutchings, Q. Lu, R. V. Forest, A. Moore and F. Jiao, *ACS Catal.*, 2015, **5**, 4586-4591.
13. A. S. Varela, N. R. Sahraie, J. Steinberg, W. Ju, H.-S. Oh and P. Strasser, *Angew. Chem. Int. Ed.*, 2015, **54**, 10758-10762.
14. H. Wang, Y. Chen, X. Hou, C. Ma and T. Tan, *Green Chem.*, 2016, **18**, 3250-3256.